JCB Journal of Cell Biology

ARTICLE

Single-particle cryo-EM reveals conformational variability of the oligomeric VCC β-barrel pore in a lipid bilayer

Nayanika Sengupta[1], Anish Kumar Mondal[2], Suman Mishra[1], Kausik Chattopadhyay[2], and Somnath Dutta[1]

***Vibrio cholerae* cytolysin (VCC) is a water-soluble, membrane-damaging, pore-forming toxin (PFT) secreted by pathogenic *V. cholerae*, which causes eukaryotic cell death by altering the plasma membrane permeability. VCC self-assembles on the cell surface and undergoes a dramatic conformational change from prepore to heptameric pore structure. Over the past few years, several high-resolution structures of detergent-solubilized PFTs have been characterized. However, high-resolution structural characterization of small β-PFTs in a lipid environment is still rare. Therefore, we used single-particle cryo-EM to characterize the structure of the VCC oligomer in large unilamellar vesicles, which is the first atomic-resolution cryo-EM structure of VCC. From our study, we were able to provide the first documented visualization of the rim domain amino acid residues of VCC interacting with lipid membrane. Furthermore, cryo-EM characterization of lipid bilayer–embedded VCC suggests interesting conformational variabilities, especially in the transmembrane channel, which could have a potential impact on the pore architecture and assist us in understanding the pore formation mechanism.**

Introduction

The pore-forming toxins (PFTs) are a class of secreted virulent proteins produced by pathogenic bacteria. PFTs assemble on the host cell plasma membrane and permeabilize the target cells by punching transmembrane holes. PFTs adopt various strategies to traverse the lipid bilayer for creating pores in biomembranes. Individual protomers of PFTs are secreted as soluble protein by pathogenic bacteria that then accumulate on the surface of the target cell membranes to form a prepore (Iacovache et al., 2012). Subsequently, the pore-forming motifs of the membrane-associated prepore span through the lipid bilayer to punch holes (Dal Peraro and van der Goot, 2016). Generally, PFTs are classified as α-PFT and β-PFT based on the 3D structure of their membrane-inserted transmembrane region (Yamashita et al., 2014; Gouaux, 1997; Parker and Feil, 2005). The transmembrane channel of α-PFTs is spanned by α-helices, while the β-PFTs are able to construct the pore by a β-barrel structure (Iacovache et al., 2010). PFTs do not just puncture holes and permeabilize cells; many also hijack housekeeping functions of the host and lead to various pathophysiological conditions, as in the case of diphtheria, anthrax, or cholera.

Vibrio cholerae cytolysin (VCC) belongs to the β-PFT family, where a β-hairpin structure of the individual protomer assembles to form a β-barrel structure. VCC is encoded by the *hlyA* gene in enterotoxic strains of *V. cholerae*. It initially folds into an 80-kD protoxin, which is processed by endogenous or exogenous proteases to form the mature toxin. Proteolytic cleavage occurs in the N-terminus of the protoxin and removes ∼15 kD of "pro-domain" (Paul and Chattopadhyay, 2011). Thus, hemolytically active VCC is an ∼65-kD monomer that can bind the host cell membrane and oligomerize into a heptameric pore of an outer diameter of ∼8 nm and inner diameter between 1 and 2 nm. It has a preference to penetrate cholesterol-rich membranes and form a seven-membered ring-like oligomeric pore structure (Harris et al., 2002).

The crystal structure of the VCC oligomeric pore solved one decade ago revealed a heptameric assembly of protomers remarkably similar to the staphylococcal toxin α-hemolysin (De and Olson, 2011). Each protomer of VCC contributes β-trefoil lectin-like domain, β-prism lectin-like domain, cytolysin domain, and the membrane-proximal rim domain, which come together and build the extracellular mushroom head-like architecture. The membrane-spanning element of the toxin is a rigid barrel composed of 14 antiparallel β-strands (De and Olson, 2011). Sequence analyses of α-hemolysin, leukocidin F, VCC, and

[1]Molecular Biophysics Unit, Indian Institute of Science, Bangalore, India; [2]Centre for Protein Science, Design and Engineering, Department of Biological Sciences, Indian Institute of Science Education and Research Mohali, Punjab, India.

Correspondence to Somnath Dutta: somnath@iisc.ac.in.

aerolysin showed that despite low sequence identity, a central 250-amino acid region of VCC was related to the three other β-PFTs (Olson and Gouaux, 2003). It was reported that VCC has its cytolytic core conserved with α-hemolysin and leukocidin F, suggesting that they follow the same pore formation mechanism (Olson and Gouaux, 2003, 2005). The crystal structure of the VCC heptamer also indicated an unexpected resemblance with anthrax toxin because of the presence of a ring of aromatic residues (W318) lining the narrowest constriction of the pore (De and Olson, 2011). In addition, various studies have impressed upon an obligatory role of cholesterol to promote lytic activity of VCC (Zitzer et al., 2000, 2001, 2003; Harris et al., 2002; Chattopadhyay et al., 2002; Ikigai et al., 2006; Paul and Chattopadhyay, 2012). Although pore-forming proteins have been studied exhaustively over the years, the repertoire of changes guiding such colossal structural rearrangements still remains an enigma. It is believed that furthering knowledge regarding the prepore intermediates may lay the foundation in understanding the precise pathway followed by these membrane-attacking oligomers. Additionally, the cryo-EM resolution revolution (Kühlbrandt, 2014) and recent developments in single-particle analysis allow us to explore the possibility to visualize this macromolecular ensemble on biomembrane in near-native state at atomic resolution. Previously, few cryo-EM structures of various detergent-solubilized PFTs have been characterized. However, only two PFTs to date have been visualized and characterized using single-particle cryo-EM and cryo-electron tomography in cholesterol-containing liposomes (Ruan et al., 2018; van Pee et al., 2017; Tilley et al., 2005; Gilbert et al., 1999).

Taking cues from the present understanding of VCC, we aimed to resolve a high-resolution cryo-EM structure of the native toxin embedded in cholesterol-enriched liposomes. Our cryo-EM map shows good agreement with the crystal structure and adds to existing knowledge with novel insights into the transmembrane β-barrel insertion mechanism. VCC embedded in the biomembrane mimetic asolectin-cholesterol liposomes were imaged at near-physiological conditions using cryo-EM, which provides the detailed structural insight of the β-barrel domain of VCC. This unambiguously highlights the amino acid residues of the β-barrel domain that directly interact with lipid moieties in the bilayer environment. Such interactions may specifically aid in membrane lipid recognition and initiate the several transitions toward pore formation. A number of additional amino acid residues observed to be coupled with the lipid density in our cryo-EM map may have a stabilizing effect and help to tether the massive extracellular part of the heptamer firmly to the membrane. Careful inspection of our cryo-EM map indicates a minor shift starting from F288 located near the mouth of the β-barrel. We speculate that this interesting phenomenon may be attributable to a bilayer membrane that could have a role in slightly altering the barrel architecture as reported in the presence of a detergent micelle. Thus, our structural findings may provide a holistic view regarding the pore formation mechanism followed by VCC and could be extended to its structurally related staphylococcal toxins, cholesterol-dependent cytolysins, and distantly related β-PFTs when present in a lipid bilayer–bound condition.

Results

Crystal structure of the detergent-solubilized heptameric pore state of VCC was resolved by De and Olson (2011). However, there is no high-resolution structure available for the VCC pore incorporated in the membrane lipid bilayer. Therefore, our main objective was to resolve the atomic-resolution structure of VCC embedded in the liposome. To accomplish our goal, we used negative staining room-temperature transmission electron microscopy (TEM) analysis and single-particle cryo-EM to image membrane-embedded VCC (Figs. 1 and 2). For this, ∼4,500 movies were collected using a 200-kV Talos Arctica cryo-electron microscope equipped with K2 direct electron detector. Only images where VCC-embedded liposomes were visible in the micrographs, and ∼1,173,994 membrane-embedded VCC single particles were automatically selected for image processing were considered (Figs. 2 and S2 A). Furthermore, we performed several rounds of rigorous 2D and 3D classifications to classify various states of VCC associated with the lipid bilayer. This cryo-EM–based structural study and powerful 3D classification technique allowed us to categorize the dataset into three major classes: (i) a structural state that was fully embedded in the lipid bilayer (representing the complete pore formation), (ii) a state in which only the part of the transmembrane scaffold partially embedded in the membrane lipid bilayer was documented, and (iii) a state that was anchored on the surface of the membrane and most of the transmembrane scaffold could not be documented/visualized (Fig. 3; Fig. S1; and Fig. S2, B and C). In the next sections, we discuss the structural features of these three structural states of VCC and lipid–protein interactions that we observed in the presence of the membrane lipid bilayer.

Negative staining TEM study to visualize the oligomeric assembly of VCC formed in the membranes

Initially, membrane-associated VCC particles were visualized using negative staining TEM, where heptameric ring-shaped complexes were observed (Fig. 1, A–D). Most of the ring-shaped complexes were tightly attached with the lipid vesicle, and no free VCC particles were observed in the background of the TEM grids. Therefore, negative staining images and 2D class averages suggested that most of the VCC heptamers were attached with the lipid vesicle and were suitable for our cryo-EM study (Fig. 1, C and D). These reference-free 2D class averages are comparable with the heptameric VCC crystal structure (Fig. 1, B–D). Previously, there has been no report of using single-particle analysis to resolve the high-resolution cryo-EM structure of small protein molecules, like VCC, embedded in the lipid vesicle. Additionally, biochemical preparation of oligomeric VCC indicates that VCC protomers were incubated with liposomes for oligomerization, and the mixture was washed with detergent-free buffer to remove the unbound VCC molecules. Thus, it is expected that only liposome-bound VCC molecules would be visible, which is supported by negative staining TEM study (Fig. 1, C and D). Therefore, our initial target was to confirm whether single-particle cryo-EM is suitable to characterize the structure of the membrane-embedded VCC molecules. We performed reference-free 2D classification of negatively stained VCC particles to identify various orientations of

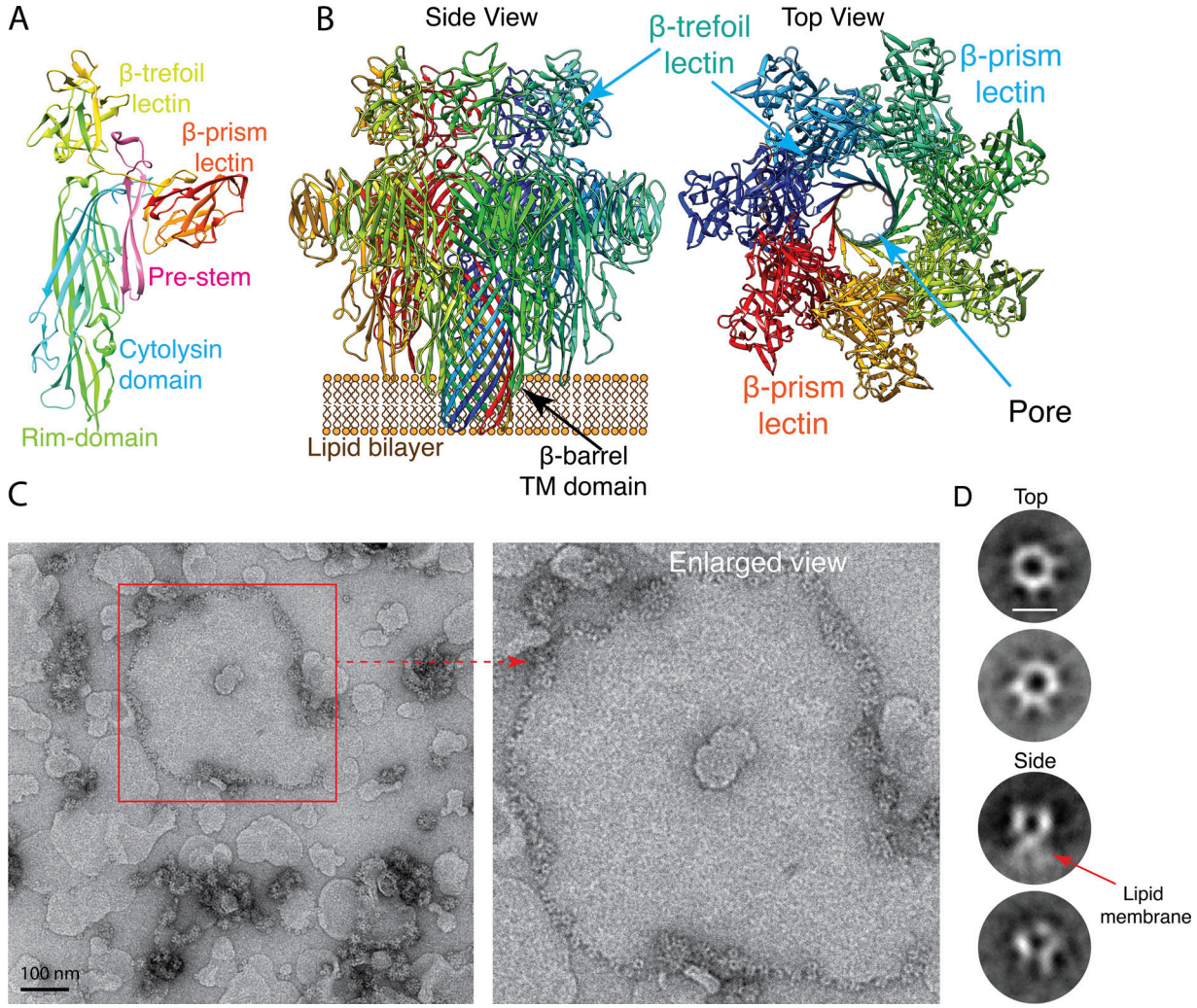

Figure 1. **Negative staining TEM analysis of large unilamellar vesicle–bound VCC. (A)** Protomer of VCC crystal structure (PDB accession no. 1XEZ) shows the five prominent domains of the toxin. **(B)** Crystal structure of detergent-solubilized VCC heptamer (PDB accession no. 3O44) represented on a cartoon membrane. A single protomer of VCC is denoted by the colored ribbons in the side and top views of the structure. **(C)** A representative negative staining micrograph shows the uniform distribution of VCC in lipid vesicles. The red boxed area has been enlarged to show the liposomes studded with oligomeric toxin complexes. **(D)** Reference-free 2D class averages show top views and membrane-embedded side views of the protein. Scale bar = 100 Å. TM, transmembrane.

the VCC molecules. Reference-free 2D classification showed top, bottom, side, and partial side views of the VCC molecules (Fig. 1, C and D). These results provided us sufficient confidence to visualize the small VCC molecules in association with the lipid vesicles at cryogenic conditions. Therefore, we decided to proceed toward structural characterization of the membrane-associated forms of VCC using a single-particle cryo-EM approach.

Near-atomic–resolution cryo-EM structures of the oligomeric assembly of VCC formed in the membranes

After several rounds of 3D classifications, we obtained three different classes of 3D reconstruction of VCC particles associated with the membrane lipid bilayer at the local resolution range of 3.7–6.5 Å: (i) the VCC oligomeric pore fully embedded in the membrane lipid bilayer, (ii) oligomeric assembly structure in which only the part of the transmembrane scaffold partially embedded in the membrane lipid bilayer was documented, and (iii) VCC oligomer anchored at the surface of the membrane in which most of the transmembrane scaffold could not be documented/visualized (Figs. 2 C and 3). The membrane-distal mushroom-shaped head parts of the heptameric assembly in all three classes were found to be structurally similar. However, the major alterations in these classes were observed at the membrane-proximal region, mainly in their β-barrel regions and the membrane-proximal rim regions. The length of the β-barrel region and the surrounding lipid environment were found to be remarkably different in all three classes (Fig. 3, B, D, and F; and Fig. S2 C). A close investigation of the cryo-EM maps indicated that the length of the β-barrel region gradually increased in these three classes of the 3D reconstructions in the following sequences: (i) from the VCC oligomer where the structure corresponding to the β-barrel embedded in the lipid bilayer could not be visualized clearly (Figs. 3 B and S2 C), (ii) to the VCC oligomer where the part of the β-barrel embedded in the membrane lipid bilayer could be visualized (Figs. 3 D and S2

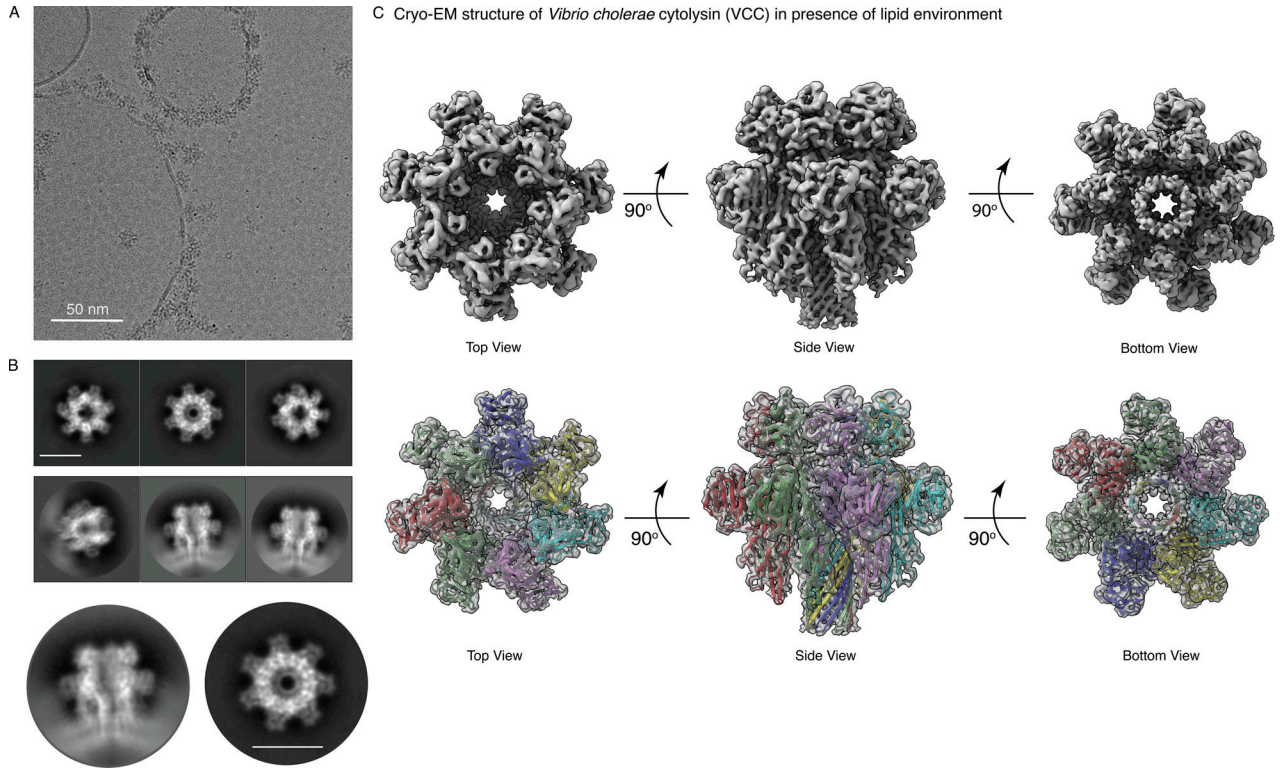

Figure 2. **Cryo-EM structure of large unilamellar vesicle–embedded VCC. (A)** A representative cryo-EM raw micrograph shows VCC oligomers firmly attached to the asolectin-cholesterol liposomes. **(B)** Reference-free 2D class averages show the wheel-like top/bottom views and the membrane-embedded side views. Enlarged representation (top panel) of the side view of the protein shows a distinct transmembrane channel spanning two leaflets of membrane. Scale bar = 100 Å. **(C)** Top, side, and bottom views of a cryo-EM 3D reconstruction of bilayer-bound VCC. Lower panel shows the fitting of the atomic model of VCC into the top, side, and bottom views of the cryo-EM density map.

C), and (iii) to the VCC oligomeric pore assembly that was found to be fully embedded in the membrane lipid bilayer (Figs. 3 F and S2 C).

In one of the classes, 3D reconstruction of the VCC oligomeric assembly was found to remain bound only at the membrane surface, and only a limited portion of the β-barrel region was visible (Fig. 3, A and B; and Fig. S2 C). In this model, two layers of lipid were visible where the β-barrel appeared to remain tethered with the first lipid layer and the length of the visible β-barrel region was small (19 Å) compared with the complete β-barrel transmembrane region (Fig. S2 C). Furthermore, the pore opening of the β-barrel at the membrane side appeared to remain blocked, presumably by the lipid bilayer (Fig. 3 A). However, the membrane-proximal rim region was successfully affixed and inserted partially within the lipid bilayer. Structural characterization of the 3D reconstruction of this class indicated that the membrane-proximal rim region of VCC interacts with the lipid membrane to provide the robust foundation of the pore formation process. It is important to note that only a small subset of 25,564 particles formed this class where the part of the β-barrel was visible, the rim region was affixed with membrane, and the membrane-proximal region of the channel was blocked by lipid layer (Figs. 3 B, S1, and S2 C).

Our study also illustrates the 3D structure of another minor class of 36,849 particles at a resolution of 5.6 Å in which the part of the β-barrel stem of the VCC oligomeric assembly was found to be partly embedded into the single lipid layer (Fig. 3, C and D; and Figs. S1, S2 C, and S3). In this structural model, a single lipid layer was visible, and the β-barrel stem was observed to pass through the first lipid layer, while the rest of the β-barrel crossing the second lipid layer could not be detected (Fig. 3 C). As a result, the membrane-proximal region of the β-barrel channel remained obstructed by lipid membrane. The length of the β-barrel region in this class is 50 Å, which is shorter than the fully oligomeric pore assembly but longer than the membrane surface–associated VCC oligomer (Fig. S2 C). Interestingly, in this structure, the membrane-proximal rim region of VCC was tightly inserted within the lipid monolayer, whereas the β-barrel stem was partially implanted through the first lipid layer. Such continuous flexibility of the β-barrel region was also supported by the 3D variability analysis of the dataset (Figs. S1 and S2 B, Video 1, and Video 2).

High-resolution cryo-EM structure of the oligomeric pore assembly of VCC with its β-barrel scaffold fully embedded in the membrane lipid bilayer

As mentioned earlier, after several rounds of 3D classifications, one cryo-EM reconstruction of the VCC oligomeric assembly in association with the liposome membranes showed the elongated β-barrel stem that passed through the membrane lipid bilayer, and this model contained 117,427 particles (Fig. 3, E and F; and Figs. 4, S1, and S2 C). The local resolution calculation indicated

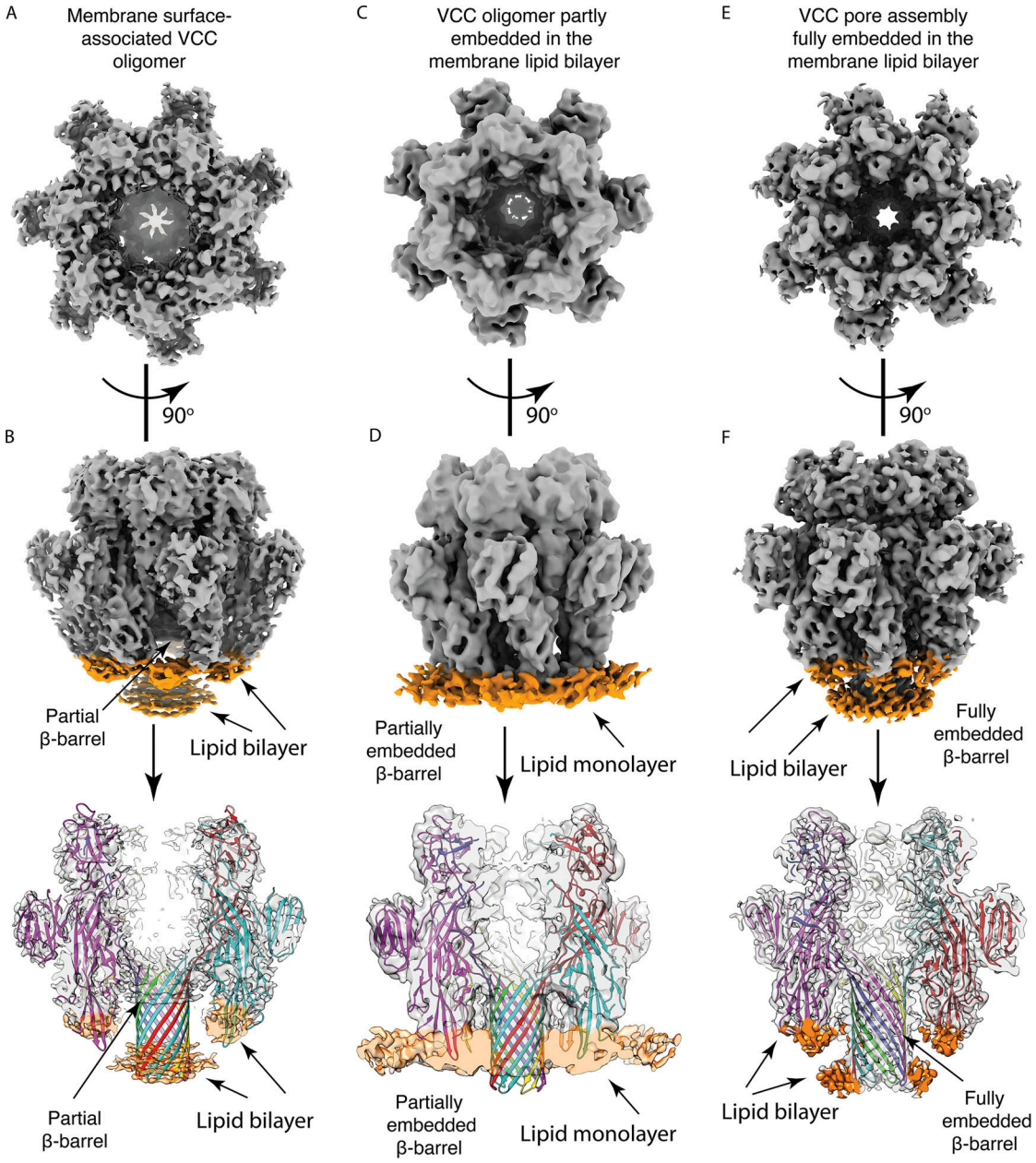

Figure 3. **Comparison of the three distinct structural states of VCC in a lipid bilayer environment. (A)** Top view of the membrane surface–associated VCC shows that the pore is blocked by the lipid layer. **(B)** Side view of the membrane surface–associated VCC shows part of the β-barrel and faint lipid density (marked orange). Fitting of the heptameric crystal structure shows a markedly small portion of the β-barrel in this cryo-EM structure. **(C)** Top view of the partially membrane-embedded VCC shows that the pore is blocked by the lipid layer. **(D)** Side view of the partially membrane-embedded VCC shows the β-barrel embedded in a disordered layer of lipid (marked orange). This class of VCC denotes a structural state where the transmembrane channel is partly bound to the lipid such that there is no perforation on the other end of the membrane. Fitting of the heptameric crystal structure shows visualization of a longer channel compared with the previous structural state. **(E)** Top view of the completely membrane-embedded VCC shows that a pore is formed in the lipid bilayer. **(F)** Side view of the completely membrane-embedded VCC shows a long transmembrane β-barrel firmly placed between two relatively ordered layers of lipid (marked orange). Fitting of the heptameric crystal structure shows proper fitting along the length of the oligomer.

that the lipid bilayer–embedded, fully formed pore model has a high resolution of 3.7–4.0 Å, and this is the first cryo-EM structure of the fully membrane-embedded VCC at atomic resolution (Fig. 2 C; Fig. 3, E and F; and Figs. 4, 5 and 6). The previous crystal structure of VCC oligomeric pore (Protein Data Bank [PDB] accession no. 3O44) solved by De and Olson (2011) could not visualize the detergent micelle. However, our cryo-EM reconstruction of the VCC oligomeric pore fully embedded in the membrane lipid bilayer reveals detailed information of the β-barrel region and rim region, where the lipid bilayer is distinctly detectable (Figs. 3 F and 5, A and B). In this cryo-EM reconstruction, two lipid layers are also clearly visible, and the β-barrel passes through the lipid bilayer. The cryo-EM model shows that the length of the overall molecules is ∼145 Å, and the

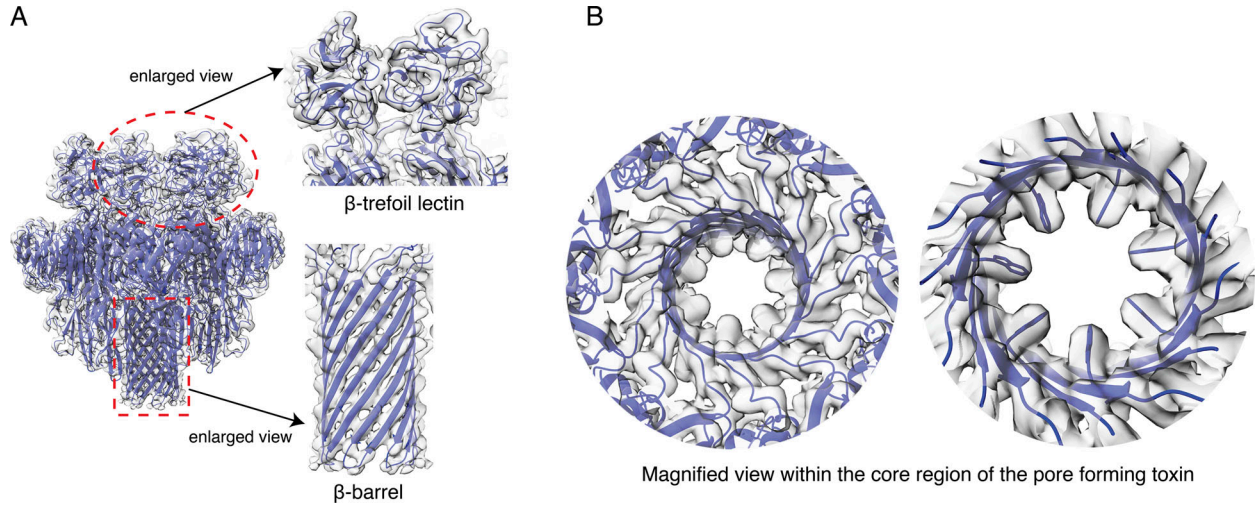

Figure 4. **Fitting of secondary structural elements in the cryo-EM density map of VCC. (A)** Side view of heptameric bilayer–bound VCC fitted with the atomic model. Enlarged views show a part of the β-trefoil region and the entire transmembrane channel. **(B)** Magnified image of the core region viewed from the top of the β-barrel. Representation of the narrowest aperture of the pore marked by seven W318 residues observed in the cryo-EM density.

length of the β-barrel transmembrane region is 64 Å (Fig. S2 C), which are similar to that reported in the previously published crystal structure (Fig. 6 A). Additionally, the rim region is firmly (~24 Å) penetrated through the lipid bilayer (Fig. 5, A and B).

Protein–lipid interactions of the rim region

From our cryo-EM structural model, we could pinpoint several amino acid residues, such as Trp420, Val422, Val423, and Trp362, in the rim region that might be responsible for lipid binding (Fig. 5, A, B, D, and E). Strikingly, we noticed that the rim region is more embedded in the lipid membranes compared with that proposed in the previously determined crystal structure (Fig. 5, D–F). Furthermore, we were able to detect all the amino acids that are embedded in the lipid membranes. Several studies indicated that a two-residue motif (Thr490 and Leu491) in the membrane-interacting region of the cholesterol-dependent cytolysins is crucial in recognizing the cholesterol moiety in the lipid membranes (Farrand et al., 2010; De and Olson, 2011). Additionally, a previous study (Rai and Chattopadhyay, 2015) showed that in the case of VCC, a similar T237–L238 motif is crucial for the membrane-binding process. Consistent with such report, we observed strong lipid density visible in the cryo-EM map in the corresponding locations. Thus, the cryo-EM model and the atomic model of VCC in this study suggest that indeed, the T237–L238 motif directly interacts with lipids and faces the lipid (Fig. 5). Furthermore, as reported in a previous study (De and Olson, 2011), several extra lipid densities were observed in the regions surrounding the loop A360–L361, thus supporting the notion that this loop also plays a vital role in the membrane interaction process. We were able to visualize clear lipid moieties, and these lipid moieties appeared to be prolonged from one protomer to another protomer (Fig. 5 D). The lipid moieties are dispersed within the several amino acid residues, like Trp362-His419/His426, Trp362-Tyr417/Tyr241, Tyr420-Trp362, and Tyr235-Phe242, identified between different VCC protomers (Fig. 5 D). In the current study, several substantial lipid densities are observed within the various amino acid residues of two protomers, like protomer 1 Trp362 with protomer 2 Tyr 241, Tyr420, Tyr421, and Tyr417. Also important to mention is that lipid moieties are observed near the two valine residues (V422 and V423) at the tip of the most extended loop of the rim region at a lower threshold level.

Transmembrane architecture of membrane bilayer–bound VCC

Our local resolution calculation indicates that the cryo-EM 3D reconstruction of the VCC oligomeric pore embedded in the membrane lipid bilayer is of significant high resolution, which is appropriate to determine the atomic model structure of the VCC pore using Phenix refinement (Fig. 2 C; and Figs. 4, 6, and S3). In accordance with past report, we have noticed that Trp318 residues are located in the β-barrel transmembrane domain initiation region, and Trp318 residues are clearly visible in the high-resolution cryo-EM map. The location of the Trp318 residues in the cryo-EM structure and crystal structure are identical. No significant displacement was noticed in the initiation region (Trp318 residues) of the β-barrel transmembrane domain. However, our study could not unravel the biological significance rendered by Trp318 residues, and past Förster resonance energy transfer study as well shows that mutation of W318F does not alter the pore-forming efficiency of VCC (Rai and Chattopadhyay, 2014). Although, no significant displacement was noticed in Trp318 residues, there is a minute 2.43 Å shift in the membrane-proximal region of the β-barrel transmembrane domain between the atomic model of the lipid bilayer–embedded VCC pore and detergent-solubilized crystal structure of VCC determined earlier (Fig. 6 A). It is important to mention that the residues Ser299, Gly300, Asp301, and Gly302 at the membrane-proximal region of the β-barrel stem appear with lipid moieties and are exceptionally disordered, presumably due to the presence of the unstable lipid layer. A similar phenomenon was observed in cryo-EM reconstruction of the lysenin pore complex and anthrax toxin pore complex, where the extreme lower half

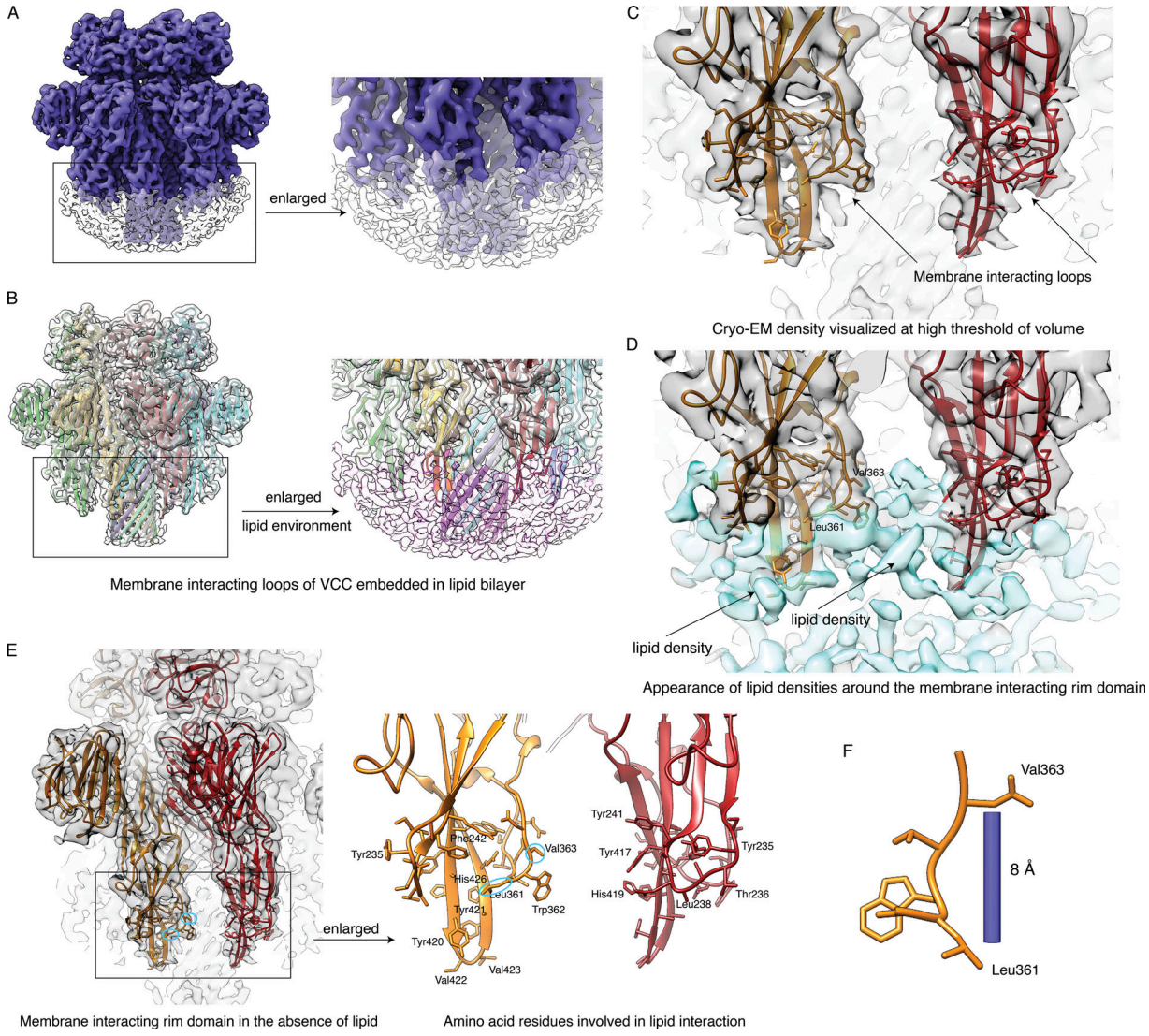

Figure 5. **Role of membrane-proximal rim domain in facilitating pore formation by VCC. (A)** Cryo-EM 3D reconstruction of liposome-bound VCC resolved at 4 Å. Protein is colored blue, and the lipid density is rendered transparent. **(B)** A transparent representation of density map fitted with the atomic model of VCC. Enlarged view shows the extent of immersion of the membrane-proximal portion of the atomic model within the lipid layer. **(C)** Two adjacent monomers of the atomic model visualized within the cryo-EM map at a high threshold of volume where lipid moieties are not observed. **(D)** A low threshold of volume shows the lipid densities intermingled with the side chains of the membrane-proximal rim domains. **(E)** Enlarged view of the cytolysin domain and the membrane-proximal rim shows amino acid residues observed to interact with the lipid moieties. **(F)** The distance between Leu361 and Val363 indicates that the rim domain is inserted by an additional 8 Å in near-physiological conditions.

of the β-barrel transmembrane region is partially disordered (Fig. S4). The similar variability was also noticed in our high-resolution, fully membrane–embedded VCC reconstruction, and the above-mentioned residues appeared as disordered. Interestingly, Val423 at the tip of the membrane-proximal rim region appears shifted (Fig. 6 A). The presence of a bilayer lipid membrane could be the reason for the extended state of the rim region. Additionally, on average, the β-trefoil domain was observed to be nominally shifted by 2.3 Å (Fig. 6 A). This structural analysis also indicates an outward movement in the β-barrel transmembrane domain and the β-trefoil domain in the lipid bilayer–embedded cryo-EM structure (Fig. 6 A). However, it could be said that overall, a strong coherence exists between the lipid bilayer–embedded cryo-EM map and the detergent micelle–purified crystal structure.

Discussion

In the current study, the first atomic-resolution cryo-EM structure of the VCC oligomeric pore assembled in the membrane lipid bilayer of liposome was resolved using single-particle analysis. This is the only structural study where small β-PFT is characterized in the presence of the real lipid membrane and reveals the lipid–protein interactions of the rim region and the β-barrel of VCC. This structural study will assist us in following a similar pipeline to characterize the small β-PFTs

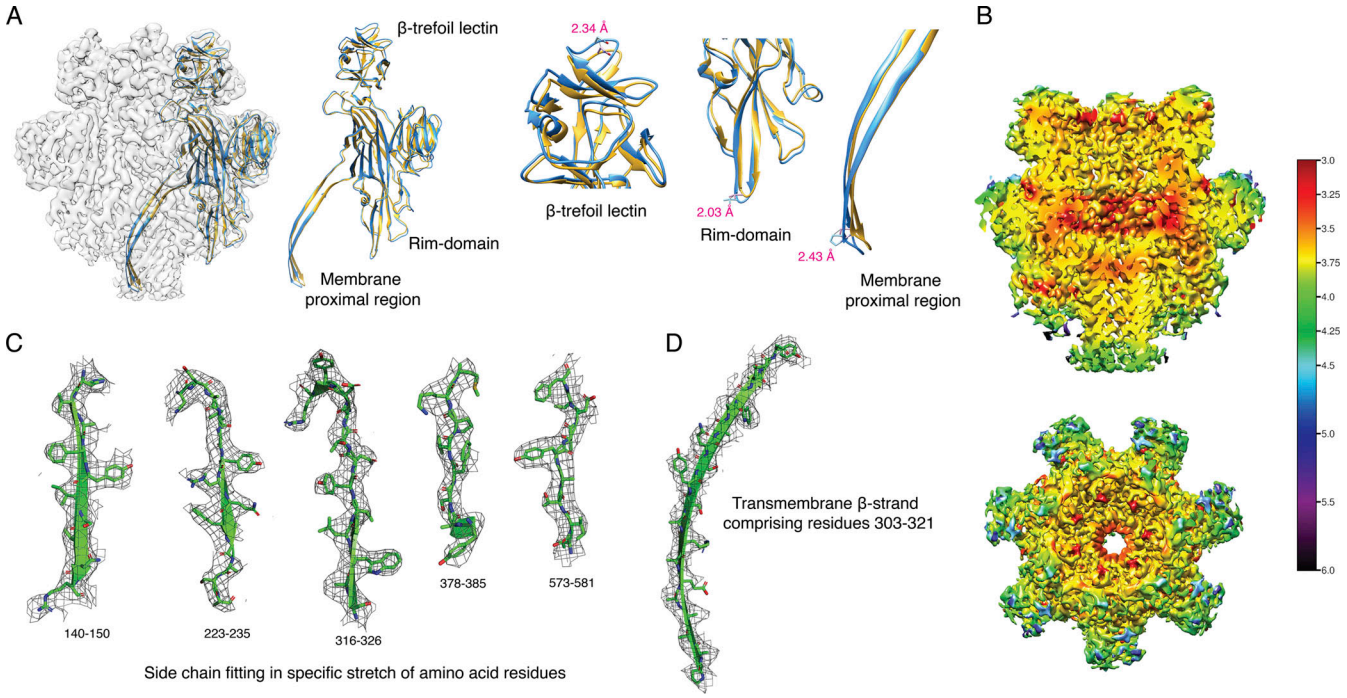

Figure 6. **Comparative analysis of the refined cryo-EM model of membrane-bound VCC with the crystal structure and local resolution estimation.** **(A)** Alignment of a single protomer of the real space-refined cryo-EM model (blue) and the crystal structure (gold) reveals nominal displacement in marked amino acid residues. **(B)** Local resolution estimation of the fully membrane-bound VCC is demonstrated by a cross section of the side view and the top view of the oligomer. **(C)** Five segments of the N chain of VCC show the quality of side chain fitting. Residues covered are 140–150, 223–235, 316–326, 378–385, and 573–581. **(D)** N-chain transmembrane β-strand spanning residues 303–321 shows the resolution of the pore-forming element.

to address the previously unattainable questions of the pore formation mechanism.

Previous x-ray crystallography–based structural study of VCC oligomeric pore was performed with detergent-solubilized protein preparation (De and Olson, 2011). However, the detergent micelle was not visible around the β-barrel transmembrane domain. Several cryo-EM structures of pores and prepore assembly of pneumolysin (van Pee et al., 2017; Tilley et al., 2005; Gilbert et al., 1999), lysenin (Bokori-Brown et al., 2016), and aerolysin (Iacovache et al., 2016) were reported previously. Additionally, Jiang et al. (2015) showed the atomic-resolution cryo-EM model of the pore assembly of anthrax toxin, where the extended β-barrel transmembrane region is distinctly visible. However, in most of the cases, oligomeric pore assembly of the PFT formed in the lipid bilayer has been solubilized using detergent for the subsequent cryo-EM–based structural study (Podobnik et al., 2016; Iacovache et al., 2016; Bräuning et al., 2018). Recently, anthrax toxin (Hardenbrook et al., 2020; Antoni et al., 2020) was characterized in the presence of lipid nanodiscs. To date, only one cryo-electron tomographic analysis of the pore assembly of pneumolysin (van Pee et al., 2017) and a few single-particle cryo-EM analyses of PFTs have been done in the presence of liposome (Gilbert et al., 1999; Tilley et al., 2005; Ruan et al., 2018; Piper et al., 2019; Pang et al., 2019). However, pneumolysin structures are low resolution (~27 Å), whereas the single-particle–based gasdermin A3 membrane pore is determined at atomic resolution. Both structures, however, are incredibly massive compared with the oligomeric pore structure of VCC. In the current study, single-particle cryo-EM was used to characterize the 3D structure of VCC oligomeric pore in the membrane environment. Thus, this unique approach implements single-particle cryo-EM structural studies to resolve the atomic models of liposome-embedded small β-barrel PFTs and identify the interactions of lipid membrane with various regions of the VCC pore assembly. Previously, several studies showed that cryo-EM and 3D classifications have significant potential to identify various conformational states of biomolecules (Abeyrathne et al., 2016; Banerjee et al., 2016; Plaschka et al., 2017; Shah et al., 2020; Wrapp et al., 2020). Based on the present understanding, it could be presumed that imaging of a large unilamellar vesicle–inserted VCC oligomeric pore at native conditions using the cryo-EM technique may reveal discrete structural entities of VCC comparable to other PFTs (Figs. S4 and S5). Our cryo-EM analysis indicates the first cryo-EM structure of VCC at atomic resolution and that the majority of the VCC particles comprise a fully membrane-embedded heptamer. This structural characterization of VCC is one of the few PFTs resolved in the presence of lipid membrane at an atomic resolution (van Pee et al., 2017; Ruan et al., 2018; Piper et al., 2019; Pang et al., 2019). In this 3D reconstruction, membrane-embedded β-barrel surrounded by lipid membranes is strongly noticeable, where the β-barrel transmembrane channel appears to pass through the lipid bilayers.

Our study provides detailed structural information of fully lipid bilayer–embedded VCC conformer, where we notice intriguing conformational changes between the cryo-EM structure

and crystal structure (De and Olson, 2011). These conformational changes are observed in the lower half of the β-barrel transmembrane region more precisely after the amino acid residue F288 in the β-barrel transmembrane channel. It is important to mention that the rim region of VCC also strongly interacts with the lipid membrane, and amino acid residues (His419–His426) of the rim region are fully incorporated into the lipid layer. Interaction of the rim region with the membrane lipid bilayer was not documented in the previously determined crystal structure of the detergent-solubilized VCC oligomeric pore. The present cryo-EM structure of VCC provides the first direct evidence that the rim region of VCC is anchored in the membrane lipid bilayer in the process of membrane pore formation. Several such residues are embedded in the outer lipid layer, which may render extra stability to the VCC pore in the membrane platform. Additionally, several other amino acid residues (Tyr235, Tyr241, Phe242, Trp362, Tyr417, Tyr420, and His426) of the cytolysin domain are tightly coupled with lipid moieties. Furthermore, our study pinpointed that the last four amino acid residues of the β-hairpin loop of the β-barrel stem are considerably disordered. A similar phenomenon is observed in the cryo-EM structure of anthrax toxin (Jiang et al., 2015) and lysenin pore (Bokori-Brown et al., 2016), where the detergent-surrounded extreme lower part of β-barrel appeared as low-resolution features and comparatively less resolved structure (Fig. S5, A–C). It is possible that some of the amino acid residues at the β-hairpin loop region of the extreme lower part of the β-barrel stem are flexible, and that might help the β-hairpin loop to cross the lipid membrane. Future studies in this direction will be required to elucidate the implications, if any, of such flexible/disordered regions of the β-barrel for pore formation in membranes.

The pore formation mechanism of the archetypical β-PFTs, including that of VCC, follows a three-step pathway to punch holes in the lipid membranes: (i) individual monomers interact with the lipid membranes and accumulate on the membrane surface, (ii) membrane-bound toxin monomers self-assemble to form intermediate prepore oligomeric structures, and (iii) prestem motif inserts through the lipid membrane to generate the stable transmembrane pore. Initiation of the membrane insertion of the β-hairpins of the pore-forming motif and transition from prepore to pore are the essential steps in the β-PFT mode of action, the mechanistic basis of which remains unclear in most cases. In addition, the exact structural disposition of the pore-forming motifs in the prepore intermediate states remains unknown for most of the β-PFTs, including VCC. Capturing the snapshots of such remarkably dynamic processes is challenging. In most of the previous studies, prepore intermediates have been trapped by introducing mutations in the protein structure and/or by altering the membrane composition. It is also possible, at least in principle, to capture the intermediate states in the process of membrane pore formation by a cryo-EM–based approach if certain fractions of the membrane-associated proteins are incapable of completing the pore-formation process.

Our cryo-EM study observed that the majority (117,427 particles) of VCC molecules could form the complete β-barrel transmembrane pores. Notably, a subpopulation of the VCC molecules represented structural states where the complete pore assembly could not be visualized. Based on visual inspection, density corresponding to the fully formed transmembrane β-barrel scaffold was not observed in these subgroups of VCC particles. Furthermore, we noticed that in one of these particle subsets (36,849 particles), some density, presumably corresponding to the part of the β-barrel transmembrane scaffold, is partially anchored in the lipid bilayer. In the other subgroup of particles (25,564 particles), structure is associated at the surface of the lipid membranes with a considerably short transmembrane barrel (Figs. S1 and S2, B and C). Similar direction of continuous flexibility in the transmembrane portion is also suggested by 3D variability analysis of the data. Based on such observation, it would be tempting to consider the possibility of whether these unique structures represent the abortive intermediates that are yet to complete the pore-formation event. However, it is important to mention that we were unable to determine the atomic-resolution models of the two auxiliary structural states, likely owing to a smaller number of particles belonging to these cohorts. Therefore, these structural models did not allow us to visualize the detailed structural disposition of the pore-forming motifs in the absence of the complete pore formation, if these are at all representing the intermediate states in the pore-formation process of VCC. Therefore, in the absence of such structural details of the pore-forming motifs, it is not possible to convincingly claim these smaller fractions of the membrane-associated VCC particles to be the intermediate states trapped in the process of membrane pore formation. Nonetheless, the current study establishes a robust foundation for possible future research where trapped intermediates of VCC (via introduction of structure-guided mutations) can be targeted for the structural characterization to elucidate the actual structural disposition of the pore-forming motifs in the prepore states.

In summary, our study elucidates for the first time the high-resolution cryo-EM structure of the oligomeric pore state of VCC in the near-physiological membrane lipid environment. From this structure, we could observe direct interaction of several amino acids of the rim region as well as the β-barrel transmembrane scaffold with the lipid moiety and noticed slight displacement of the β-hairpin loop. Therefore, this study provides important new insights regarding the assembly process of the oligomeric pore state of VCC in the membrane lipid bilayer toward execution of its membrane-damaging action.

Materials and methods

Preparation of liposome-embedded VCC

Wild-type pro-VCC sequence was cloned between NdeI and BamHI restriction enzyme sites into pET-14b vector (Novagen; Merck Millipore [forward primer 5′-TGTAGTCATATG AATATCAATGAACCAAGTGGTGA-3′ and reverse primer 5′-ACAAGTGGATCCTTAGTTCAAATCAAATTGAACCCCT-3′]) and transformed into *Escherichia coli* Origami B cells (Novagen) for recombinant protein expression and purification (Paul and Chattopadhyay, 2011). Concisely, cells were grown to mid-log phase, and protein expression was induced in the presence of 1 mM IPTG at 30°C for 3 h. 6× histidine-tagged recombinant

pro-VCC was purified by Ni-nitrilotriacetic acid (QIAGEN) affinity chromatography followed by Q-Sepharose anion-exchange chromatography (GE Healthcare). To obtain the mature form of VCC, proteolytic cleavage of the pro domain was performed by treating the purified protein with trypsin in a ratio of 2,000: 1 (wt/wt) for 5 min at 25°C. Following trypsin digestion, mature VCC toxin was further subjected to another round of Q-Sepharose anion-exchange chromatography.

Asolectin-cholesterol liposomes (1:1 wt/wt) were prepared by a method described previously (Paul and Chattopadhyay, 2012). Nearly 6 µM VCC was incubated with 1,000 µg of liposomes at 25°C for 1 h. Treatment was followed by ultracentrifugation at 105,000 *g* for 30 min. Supernatant was discarded, and the pellet was resuspended in 200 µl buffer containing 10 mM Tris-HCl (pH 8.0) and 150 mM NaCl and stored at −20°C for subsequent negative staining TEM imaging.

Sample preparation and data collection for negative staining TEM

Wild-type VCC reconstituted in liposomes was assessed for overall sample homogeneity and particle distribution using negative staining TEM. Carbon-coated Cu grids were glow discharged for 30 s in a GloQube (Quorum Technologies Ltd.) glow discharge system before sample addition. 3.5 µl of 0.1 mg/ml VCC-liposome sample was added to the Cu TEM grids and incubated at room temperature for 1.5 min. Excess sample was mildly blotted off, and negative staining was performed with freshly prepared 1% uranyl acetate solution. Data were acquired at room temperature on a 120-kV FEI Tecnai T12 electron microscope equipped with Velita (2k × 2k) side-mounted TEM CCD camera (Olympus) at ×80,000 magnification and calibrated pixel size of 2.54 Å/pixel.

Negative staining TEM data processing

The micrographs were imported into EMAN2.1 software (Tang et al., 2007) for further evaluation. Approximately 1,850 liposome-embedded VCC particles were manually picked, and the coordinates were extracted using e2boxer.py in EMAN2.1. Reference-free 2D classification of the projections was performed using simple_prime2D of SIMPLE 2.0 software (Elmlund and Elmlund, 2012).

Cryo-EM sample preparation and data collection

QUANTIFOIL R1.2/1.3 300 mesh gold grids were glow discharged in a GloQube (Quorum Technologies Ltd.) glow discharge system for 130 s at 20 mA before sample addition. 3 µl of liposome-embedded VCC sample was added to freshly hydrophilized cryo-EM grids and incubated for 10 s. Excess sample was blotted for 5.5 s at 100% humidity and rapidly plunged into liquid ethane using an FEI Vitrobot IV plunger. Cryo-EM data were acquired at cryogenic temperature using a Thermo Fisher Scientific 200-kV Talos Arctica TEM equipped with K2 Summit direct electron detector (Gatan Inc.). Automated image acquisition was performed using LatitudeS (Kumar et al., 2021) automatic data collection software (Gatan Inc.) at nominal magnification of ×42,000 and pixel size 1.17 Å at specimen level. Total electron dose of ∼40 $e^-/Å^2$ between the defocus range of −0.75 µm and −2.5 µm at a calibrated dose of ∼1 $e^-/Å^2$ per frame was subjected to the sample. Data were recorded for 8 s for a total of 40 frames. Approximately 4,500 movies were collected for data processing.

Cryo-EM data processing and 3D reconstruction

4,500 movies were imported into RELION 3.1 (Scheres, 2012), and beam-induced motion correction with all the frames was performed using MotionCor2 (Zheng et al., 2017). The motion-corrected micrographs were screened in cisTEM (Grant et al., 2018), and data with the best signal-to-noise ratio were retained for further processing. However, multiple rounds of beam-induced motion correction were performed to remove initial and last frames to improve the drift of huge liposomes. Finally, the first three frames were removed to perform motion correction using MotionCor2 to gain the maximum resolution. CTFFIND 4.1.13 (Rohou and Grigorieff, 2015) was used to estimate the contrast transfer function. Initially, particles were manually picked in RELION 3.1, and reference-free 2D class averages were calculated. The best 2D class averages were selected as a template for autopicking 3,733 final micrographs. A total of 1,173,994 particles were obtained, and 2D classification was run iteratively to clean the dataset. Approximately 406,275 best particles were selected and split into 12 classes with C7 symmetry (Fig. S2). 3D classification identified several distinct classes with respect to the lipid environment. The same particles were imported into cryoSPARC 3.2 (Punjani et al., 2017), and 3D variability analysis (Punjani and Fleet, 2021) was run over 20 frames. The resolutions of individual classes were observed from 2D cross sections of 3D models and metadata of 3D classification. High-resolution models were selected for final refinement. 3D autorefinement for each class was performed with a soft mask created in RELION 3.1. Contrast transfer function refinement for each particle subset was performed with correcting anisotropic magnification, beamtilt, per-particle defocus, and per-particle astigmatism. Particles were subjected to Bayesian polishing; the "shiny" particles were imported into cryoSPARC 3.2; and homogeneous refinement was performed to yield final reconstructions at 5.3 Å, 5.6 Å, and 4.0 Å (Fourier shell correlation [FSC] 0.143) with 25,564, 36,849, and 117,427 particles, respectively. Local resolution was estimated using Blocres (Heymann, 2018). Density modification of bilayer-bound VCC was done with the ResolveCryoEM program (Terwilliger et al., 2020). All 3D structural visualizations were performed in UCSF Chimera (Pettersen et al., 2004) and UCSF ChimeraX (Goddard et al., 2018).

Real-space refinement and structural analysis

The fully lipid membrane–embedded reconstruction resolved at 4.0 Å was docked with PDB accession no. 3O44 in UCSF Chimera to perform rigid body fitting. PDB accession no. 3O44 was further taken as an initial model for phenix.dock_in_map in Phenix (Adams et al., 2010) followed by a refinement with respect to the cryo-EM map using phenix.real_space_refine. The atomic models of VCC were next compared in UCSF Chimera.

Online supplemental material

Fig. S1 shows extended 2D class averages highlighting the membrane–protein interaction of VCC heptamers and the

different 3D structural states obtained in the context of a lipid bilayer. Fig. S2 provides an overview of the cryo-EM data processing pipeline followed for 3D reconstruction and the continuous flexibility observed in the transmembrane channel of lipid bilayer–bound VCC. Fig. S3 includes the gold standard FSC calculation, local resolution estimation, and Euler angle sampling plot of the structural states of VCC. Fig. S4 shows a comparative analysis of the disorder observed in membrane proximal structural elements of PFTs. Fig. S5 represents the association of lipid moieties with the membrane-interacting domains of PFTs. Video 1 demonstrates the 3D variability of lipid bilayer–embedded VCC as visualized from the side of the protein oligomer. Video 2 demonstrates the 3D variability of lipid bilayer–embedded VCC as visualized from the top of the protein oligomer.

Data availability

The cryo-EM density maps of the three structural states of membrane bilayer-bound VCC are available from the Electron Microscopy Data Bank (under accession nos. EMD-31973 [membrane surface-adhered VCC], EMD-31974 [partially membrane-bound VCC], and EMD-31972 [fully membrane-embedded VCC]).

Acknowledgments

We thank Anil Kumar for preparing cryo-EM grids and for cryo-EM data collection.

We acknowledge the Department of Biotechnology, Ministry of Science and Technology, India (DBT); Department of Science and Technology, Ministry of Science and Technology, India (DST); and Ministry of Human Resource Development, India, for funding the cryo-EM facility at the Indian Institute of Science. Indian Institute of Science Education and Research Mohali is also acknowledged for funding support. We acknowledge the DBT-BUILDER program (BT/INF/22/SP22844/2017) and DST-FIST program (SR/FST/LSII-039/2015) for funding the cryo-EM facility at the Indian Institute of Science. We acknowledge financial support from the Ministry of Human Resource Development (grant no. STARS-1/171), Science and Engineering Research Board (grant nos. SB/S2/RJN-145/2015, SERB-EMR/2016/000608), and DBT (grant no. BT/PR25580/BRB/10/1619/2017) for consumables.

The authors declare no competing financial interests.

Author contributions: N. Sengupta: data curation, investigation, formal analysis, validation, visualization, writing–original draft, and review and editing. A.K. Mondal: data curation and writing–review and editing. S. Mishra: formal analysis, investigation, validation, visualization, and writing–review and editing. K. Chattopadhyay: conceptualization, methodology, supervision, writing–original draft, and review and editing. S. Dutta: conceptualization, methodology, funding acquisition, data curation, formal analysis, project administration, supervision, validation, visualization, writing–original draft, and review and editing.

Submitted: 15 February 2021
Revised: 25 August 2021
Accepted: 19 September 2021

References

Abeyrathne, P.D., C.S. Koh, T. Grant, N. Grigorieff, and A.A. Korostelev. 2016. Ensemble cryo-EM uncovers inchworm-like translocation of a viral IRES through the ribosome. *eLife.* 5:e14874. https://doi.org/10.7554/eLife.14874

Adams, P.D., P.V. Afonine, G. Bunkóczi, V.B. Chen, I.W. Davis, N. Echols, J.J. Headd, L.-W. Hung, G.J. Kapral, R.W. Grosse-Kunstleve, et al. 2010. PHENIX: A comprehensive Python-based system for macromolecular structure solution. *Acta Crystallogr. D Biol. Crystallogr.* 66:213–221. https://doi.org/10.1107/S0907444909052925

Antoni, C., D. Quentin, A.E. Lang, K. Aktories, C. Gatsogiannis, and S. Raunser. 2020. Cryo-EM structure of the fully-loaded asymmetric anthrax lethal toxin in its heptameric pre-pore state. *PLoS Pathog.* 16: e1008530. https://doi.org/10.1371/journal.ppat.1008530

Banerjee, S., A. Bartesaghi, A. Merk, P. Rao, S.L. Bulfer, Y. Yan, N. Green, B. Mroczkowski, R.J. Neitz, P. Wipf, et al. 2016. 2.3 Å resolution cryo-EM structure of human p97 and mechanism of allosteric inhibition. *Science.* 351:871–875.

Bokori-Brown, M., T.G. Martin, C.E. Naylor, A.K. Basak, R.W. Titball, and C.G. Savva. 2016. Cryo-EM structure of lysenin pore elucidates membrane insertion by an aerolysin family protein. *Nat. Commun.* 7:11293. https://doi.org/10.1038/ncomms11293

Bräuning, B., E. Bertosin, F. Praetorius, C. Ihling, A. Schatt, A. Adler, K. Richter, A. Sinz, H. Dietz, and M. Groll. 2018. Structure and mechanism of the two-component α-helical pore-forming toxin YaxAB. *Nat. Commun.* 9:1806. https://doi.org/10.1038/s41467-018-04139-2

Chattopadhyay, K., D. Bhattacharyya, and K.K. Banerjee. 2002. *Vibrio cholerae* hemolysin. Implication of amphiphilicity and lipid-induced conformational change for its pore-forming activity. *Eur. J. Biochem.* 269: 4351–4358. https://doi.org/10.1046/j.1432-1033.2002.03137.x

Dal Peraro, M., and F.G. van der Goot. 2016. Pore-forming toxins: Ancient, but never really out of fashion. *Nat. Rev. Microbiol.* 14:77–92. https://doi.org/10.1038/nrmicro.2015.3

De, S., and R. Olson. 2011. Crystal structure of the Vibrio cholerae cytolysin heptamer reveals common features among disparate pore-forming toxins. *Proc. Natl. Acad. Sci. USA.* 108:7385–7390. https://doi.org/10.1073/pnas.1017442108

Elmlund, D., and H. Elmlund. 2012. SIMPLE: Software for ab initio reconstruction of heterogeneous single-particles. *J. Struct. Biol.* 180:420–427. https://doi.org/10.1016/j.jsb.2012.07.010

Farrand, A.J., S. LaChapelle, E.M. Hotze, A.E. Johnson, and R.K. Tweten. 2010. Only two amino acids are essential for cytolytic toxin recognition of cholesterol at the membrane surface. *Proc. Natl. Acad. Sci. USA.* 107: 4341–4346. https://doi.org/10.1073/pnas.0911581107

Gilbert, R.J., J.L. Jiménez, S. Chen, I.J. Tickle, J. Rossjohn, M. Parker, P.W. Andrew, and H.R. Saibil. 1999. Two structural transitions in membrane pore formation by pneumolysin, the pore-forming toxin of Streptococcus pneumoniae. *Cell.* 97:647–655. https://doi.org/10.1016/S0092-8674(00)80775-8

Goddard, T.D., C.C. Huang, E.C. Meng, E.F. Pettersen, G.S. Couch, J.H. Morris, and T.E. Ferrin. 2018. UCSF ChimeraX: Meeting modern challenges in visualization and analysis. *Protein Sci.* 27:14–25. https://doi.org/10.1002/pro.3235

Gouaux, E. 1997. Channel-forming toxins: Tales of transformation. *Curr. Opin. Struct. Biol.* 7:566–573. https://doi.org/10.1016/S0959-440X(97)80123-6

Grant, T., A. Rohou, and N. Grigorieff. 2018. *cis*TEM, user-friendly software for single-particle image processing. *eLife.* 7:e35383. https://doi.org/10.7554/eLife.35383

Hardenbrook, N.J., S. Liu, K. Zhou, K. Ghosal, Z. Hong Zhou, and B.A. Krantz. 2020. Atomic structures of anthrax toxin protective antigen channels bound to partially unfolded lethal and edema factors. *Nat. Commun.* 11: 840. https://doi.org/10.1038/s41467-020-14658-6

Harris, J.R., S. Bhakdi, U. Meissner, D. Scheffler, R. Bittman, G. Li, A. Zitzer, and M. Palmer. 2002. Interaction of the Vibrio cholerae cytolysin (VCC) with cholesterol, some cholesterol esters, and cholesterol derivatives: A TEM study. *J. Struct. Biol.* 139:122–135. https://doi.org/10.1016/S1047-8477(02)00563-4

Heymann, J.B. 2018. Guidelines for using Bsoft for high resolution reconstruction and validation of biomolecular structures from electron micrographs. *Protein Sci.* 27:159–171. https://doi.org/10.1002/pro.3293

Iacovache, I., M. Bischofberger, and F.G. van der Goot. 2010. Structure and assembly of pore-forming proteins. *Curr. Opin. Struct. Biol.* 20:241–246. https://doi.org/10.1016/j.sbi.2010.01.013

Iacovache, I., M.T. Degiacomi, and F.G. van der Goot. 2012. 5.9 Pore-forming toxins. *In* Comprehensive Biophysics. E.H Egelman, editor. Elsevier,

Amsterdam. 164–188. https://doi.org/10.1016/B978-0-12-374920-8.00518-X
Iacovache, I., S. De Carlo, N. Cirauqui, M. Dal Peraro, F.G. van der Goot, and B. Zuber. 2016. Cryo-EM structure of aerolysin variants reveals a novel protein fold and the pore-formation process. *Nat. Commun.* 7:12062. https://doi.org/10.1038/ncomms12062
Ikigai, H., H. Otsuru, K. Yamamoto, and T. Shimamura. 2006. Structural requirements of cholesterol for binding to Vibrio cholerae hemolysin. *Microbiol. Immunol.* 50:751–757. https://doi.org/10.1111/j.1348-0421.2006.tb03848.x
Jiang, J., B.L. Pentelute, R.J. Collier, and Z.H. Zhou. 2015. Atomic structure of anthrax protective antigen pore elucidates toxin translocation. *Nature.* 521:545–549. https://doi.org/10.1038/nature14247
Kühlbrandt, W. 2014. Cryo-EM enters a new era. *eLife.* 3:e03678. https://doi.org/10.7554/eLife.03678
Kumar, A., S. P, S. Gulati, and S. Dutta. 2021. User-friendly, high-throughput, and fully automated data acquisition software for single-particle cryo-electron microscopy. *J. Vis. Exp.* (173):e62832. https://doi.org/10.3791/62832
Olson, R., and E. Gouaux. 2003. Vibrio cholerae cytolysin is composed of an alpha-hemolysin-like core. *Protein Sci.* 12:379–383. https://doi.org/10.1110/ps.0231703
Olson, R., and E. Gouaux. 2005. Crystal structure of the Vibrio cholerae cytolysin (VCC) pro-toxin and its assembly into a heptameric transmembrane pore. *J. Mol. Biol.* 350:997–1016. https://doi.org/10.1016/j.jmb.2005.05.045
Pang, S.S., C. Bayly-Jones, M. Radjainia, B.A. Spicer, R.H.P. Law, A.W. Hodel, E.S. Parsons, S.M. Ekkel, P.J. Conroy, G. Ramm, et al. 2019. The cryo-EM structure of the acid activatable pore-forming immune effector macrophage-expressed gene 1. *Nat. Commun.* 10:4288. https://doi.org/10.1038/s41467-019-12279-2
Parker, M.W., and S.C. Feil. 2005. Pore-forming protein toxins: From structure to function. *Prog. Biophys. Mol. Biol.* 88:91–142. https://doi.org/10.1016/j.pbiomolbio.2004.01.009
Paul, K., and K. Chattopadhyay. 2011. Unfolding distinguishes the Vibrio cholerae cytolysin precursor from the mature form of the toxin. *Biochemistry.* 50:3936–3945. https://doi.org/10.1021/bi200332g
Paul, K., and K. Chattopadhyay. 2012. Single point mutation in Vibrio cholerae cytolysin compromises the membrane pore-formation mechanism of the toxin. *FEBS J.* 279:4039–4051. https://doi.org/10.1111/j.1742-4658.2012.08809.x
Pettersen, E.F., T.D. Goddard, C.C. Huang, G.S. Couch, D.M. Greenblatt, E.C. Meng, and T.E. Ferrin. 2004. UCSF Chimera--a visualization system for exploratory research and analysis. *J. Comput. Chem.* 25:1605–1612. https://doi.org/10.1002/jcc.20084
Piper, S.J., L. Brillault, R. Rothnagel, T.I. Croll, J.K. Box, I. Chassagnon, S. Scherer, K.N. Goldie, S.A. Jones, F. Schepers, et al. 2019. Cryo-EM structures of the pore-forming A subunit from the Yersinia entomophaga ABC toxin. *Nat. Commun.* 10:1952. https://doi.org/10.1038/s41467-019-09890-8
Plaschka, C., P.-C. Lin, and K. Nagai. 2017. Structure of a pre-catalytic spliceosome. *Nature.* 546:617–621. https://doi.org/10.1038/nature22799
Podobnik, M., P. Savory, N. Rojko, M. Kisovec, N. Wood, R. Hambley, J. Pugh, E.J. Wallace, L. McNeill, M. Bruce, et al. 2016. Crystal structure of an invertebrate cytolysin pore reveals unique properties and mechanism of assembly. *Nat. Commun.* 7:11598. https://doi.org/10.1038/ncomms11598
Punjani, A., and D.J. Fleet. 2021. 3D variability analysis: Resolving continuous flexibility and discrete heterogeneity from single particle cryo-EM. *J. Struct. Biol.* 213:107702. https://doi.org/10.1016/j.jsb.2021.107702
Punjani, A., J.L. Rubinstein, D.J. Fleet, and M.A. Brubaker. 2017. cryoSPARC: Algorithms for rapid unsupervised cryo-EM structure determination. *Nat. Methods.* 14:290–296. https://doi.org/10.1038/nmeth.4169
Rai, A.K., and K. Chattopadhyay. 2014. Trapping of Vibrio cholerae cytolysin in the membrane-bound monomeric state blocks membrane insertion and functional pore formation by the toxin. *J. Biol. Chem.* 289:16978–16987. https://doi.org/10.1074/jbc.M114.567099
Rai, A.K., and K. Chattopadhyay. 2015. Revisiting the membrane interaction mechanism of a membrane-damaging β-barrel pore-forming toxin Vibrio cholerae cytolysin. *Mol. Microbiol.* 97:1051–1062. https://doi.org/10.1111/mmi.13084
Rohou, A., and N. Grigorieff. 2015. CTFFIND4: Fast and accurate defocus estimation from electron micrographs. *J. Struct. Biol.* 192:216–221. https://doi.org/10.1016/j.jsb.2015.08.008
Ruan, J., S. Xia, X. Liu, J. Lieberman, and H. Wu. 2018. Cryo-EM structure of the gasdermin A3 membrane pore. *Nature.* 557:62–67. https://doi.org/10.1038/s41586-018-0058-6
Scheres, S.H.W. 2012. RELION: Implementation of a Bayesian approach to cryo-EM structure determination. *J. Struct. Biol.* 180:519–530. https://doi.org/10.1016/j.jsb.2012.09.006
Shah, P.N.M., D.J. Filman, K.S. Karunatilaka, E.L. Hesketh, E. Groppelli, M. Strauss, and J.M. Hogle. 2020. Cryo-EM structures reveal two distinct conformational states in a picornavirus cell entry intermediate. *PLoS Pathog.* 16:e1008920. https://doi.org/10.1371/journal.ppat.1008920
Tang, G., L. Peng, P.R. Baldwin, D.S. Mann, W. Jiang, I. Rees, and S.J. Ludtke. 2007. EMAN2: An extensible image processing suite for electron microscopy. *J. Struct. Biol.* 157:38–46. https://doi.org/10.1016/j.jsb.2006.05.009
Terwilliger, T.C., S.J. Ludtke, R.J. Read, P.D. Adams, and P.V. Afonine. 2020. Improvement of cryo-EM maps by density modification. *Nat. Methods.* 17:923–927. https://doi.org/10.1038/s41592-020-0914-9
Tilley, S.J., E.V. Orlova, R.J.C. Gilbert, P.W. Andrew, and H.R. Saibil. 2005. Structural basis of pore formation by the bacterial toxin pneumolysin. *Cell.* 121:247–256. https://doi.org/10.1016/j.cell.2005.02.033
van Pee, K., A. Neuhaus, E. D'Imprima, D.J. Mills, W. Kühlbrandt, and Ö. Yildiz. 2017. CryoEM structures of membrane pore and prepore complex reveal cytolytic mechanism of pneumolysin. *eLife.* 6:e23644. https://doi.org/10.7554/eLife.23644
Wrapp, D., N. Wang, K.S. Corbett, J.A. Goldsmith, C.-L. Hsieh, O. Abiona, B.S. Graham, and J.S. McLellan. 2020. Cryo-EM structure of the 2019-nCoV spike in the prefusion conformation. *Science.* 367:1260–1263. https://doi.org/10.1126/science.abb2507
Yamashita, D., T. Sugawara, M. Takeshita, J. Kaneko, Y. Kamio, I. Tanaka, Y. Tanaka, and M. Yao. 2014. Molecular basis of transmembrane beta-barrel formation of staphylococcal pore-forming toxins. *Nat. Commun.* 5:4897. https://doi.org/10.1038/ncomms5897
Zheng, S.Q., E. Palovcak, J.-P. Armache, K.A. Verba, Y. Cheng, and D.A. Agard. 2017. MotionCor2: Anisotropic correction of beam-induced motion for improved cryo-electron microscopy. *Nat. Methods.* 14:331–332. https://doi.org/10.1038/nmeth.4193
Zitzer, A., J.R. Harris, S.E. Kemminer, O. Zitzer, S. Bhakdi, J. Muething, and M. Palmer. 2000. Vibrio cholerae cytolysin: assembly and membrane insertion of the oligomeric pore are tightly linked and are not detectably restricted by membrane fluidity. *Biochim. Biophys. Acta.* 1509:264–274. https://doi.org/10.1016/S0005-2736(00)00303-5
Zitzer, A., R. Bittman, C.A. Verbicky, R.K. Erukulla, S. Bhakdi, S. Weis, A. Valeva, and M. Palmer. 2001. Coupling of cholesterol and cone-shaped lipids in bilayers augments membrane permeabilization by the cholesterol-specific toxins streptolysin O and Vibrio cholerae cytolysin. *J. Biol. Chem.* 276:14628–14633. https://doi.org/10.1074/jbc.M100241200
Zitzer, A., E.J. Westover, D.F. Covey, and M. Palmer. 2003. Differential interaction of the two cholesterol-dependent, membrane-damaging toxins, streptolysin O and Vibrio cholerae cytolysin, with enantiomeric cholesterol. *FEBS Lett.* 553:229–231. https://doi.org/10.1016/S0014-5793(03)01023-8

Supplemental material

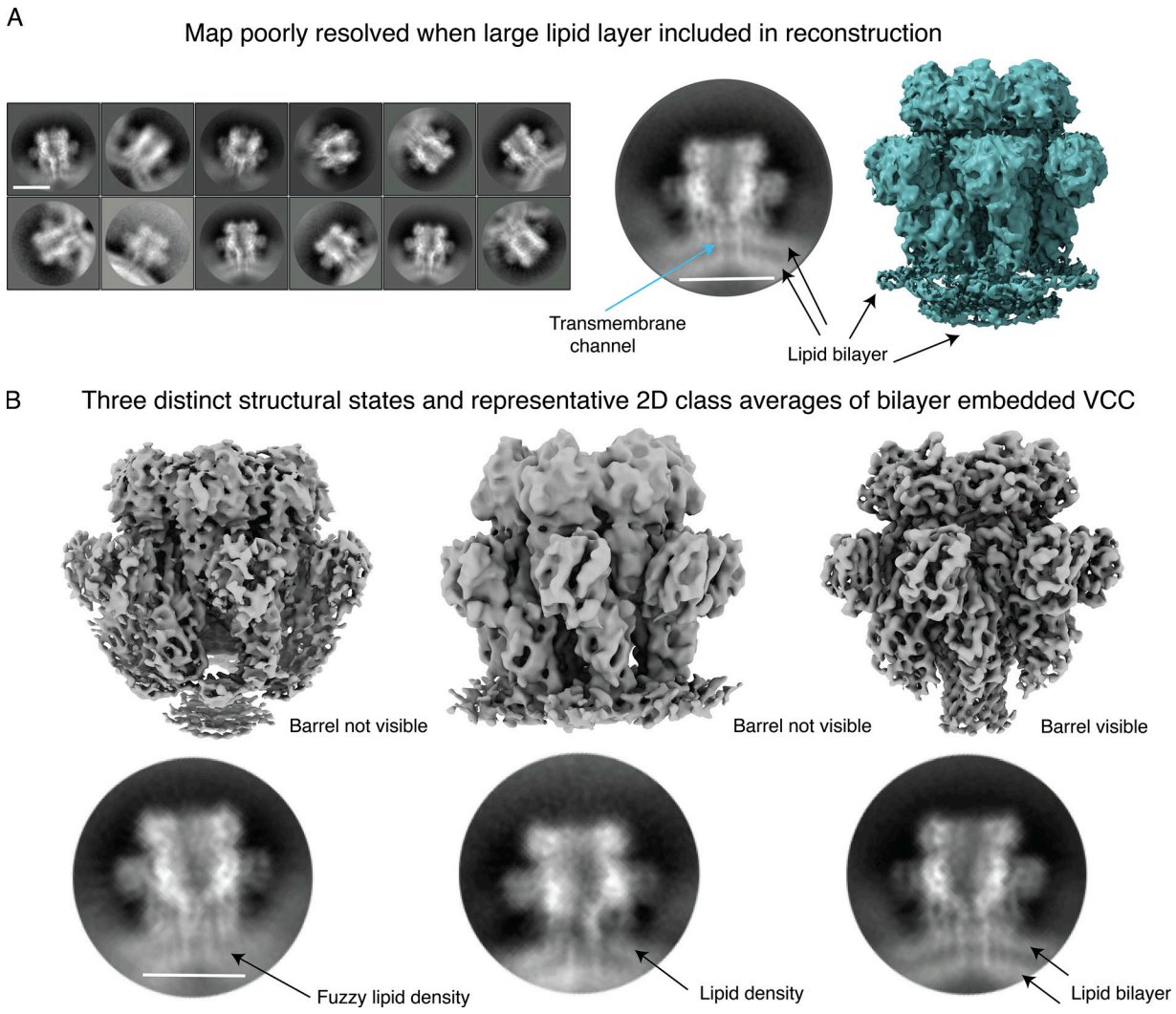

Figure S1. **Extended 2D class averages and three unique structural states of membrane-bound VCC. (A)** A panel showing only side views of the 2D projections where the PFT molecules are seen tethered between bilayers of asolectin-cholesterol liposomes. An enlarged view shows the transmembrane channel passing through the two layers of lipid density. A 3D reconstruction of VCC obtained at 5.15 Å in the presence of a large volume of lipid. **(B)** 3D volumes of the different structural states of VCC and 2D class averages (enlarged from panel A) of membrane-bound VCC suggest different extents of lipid interaction of the oligomer. Scale bar = 100 Å.

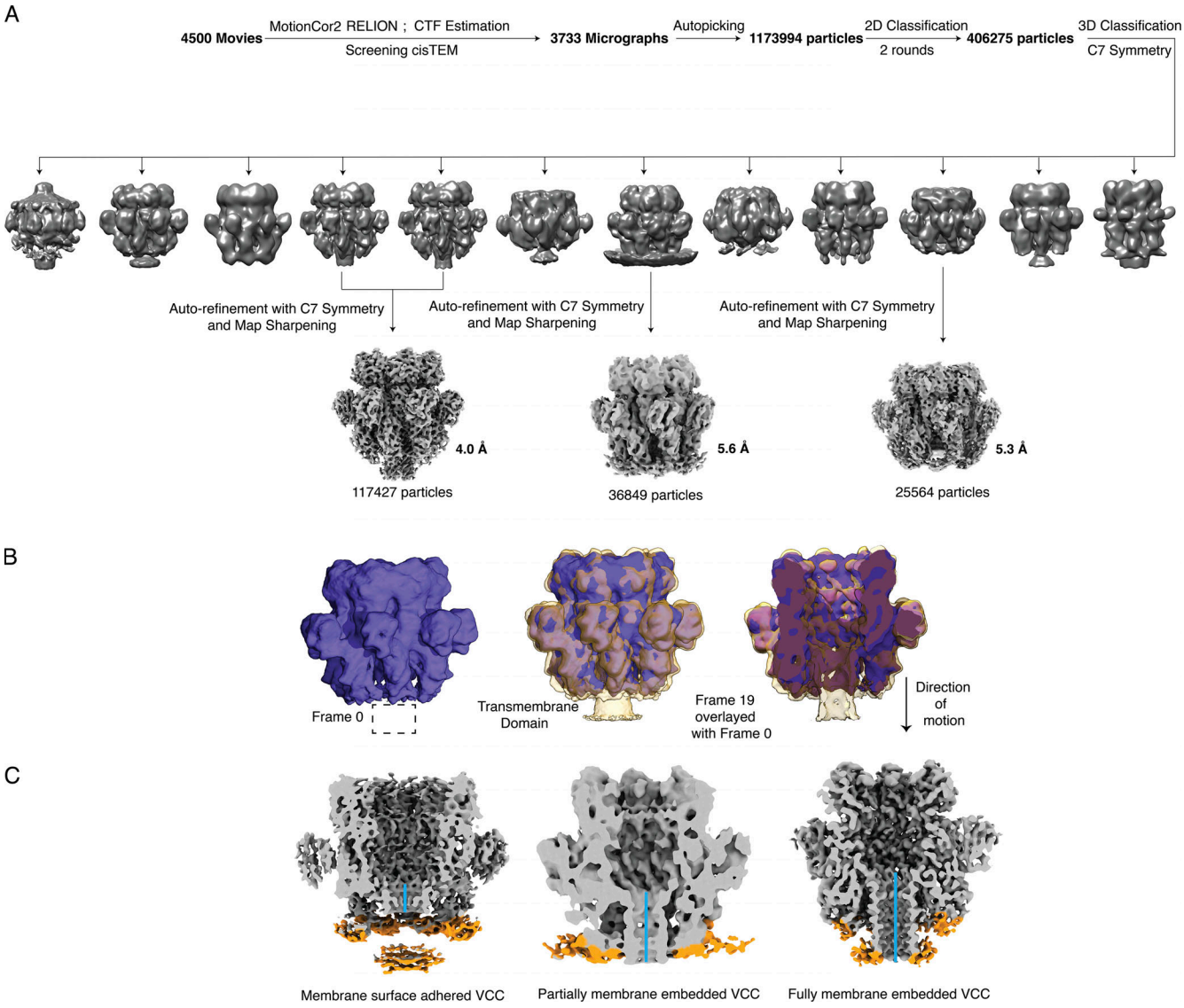

Figure S2. **Overview of cryo-EM data processing pipeline and 3D variability analysis of the liposome-embedded VCC particles. (A)** 3D reconstruction workflow of VCC embedded in liposomes. See Materials and methods for more details. **(B)** EM density corresponding to frame 0 of component 1. The dashed box shows the missing density of the β-barrel. Adjacent figure shows an overlay of frame 19 (yellow) with frame 0 (purple). Cross-sectional view of the overlaid maps indicates the direction of flexibility in the VCC particles. **(C)** Cross-sectional views of the three distinct structural states represent the size heterogeneity of the β-barrel. A blue scale bar is added corresponding to the size of 19 Å, 50 Å, and 64 Å, respectively. CTF, contrast transfer function.

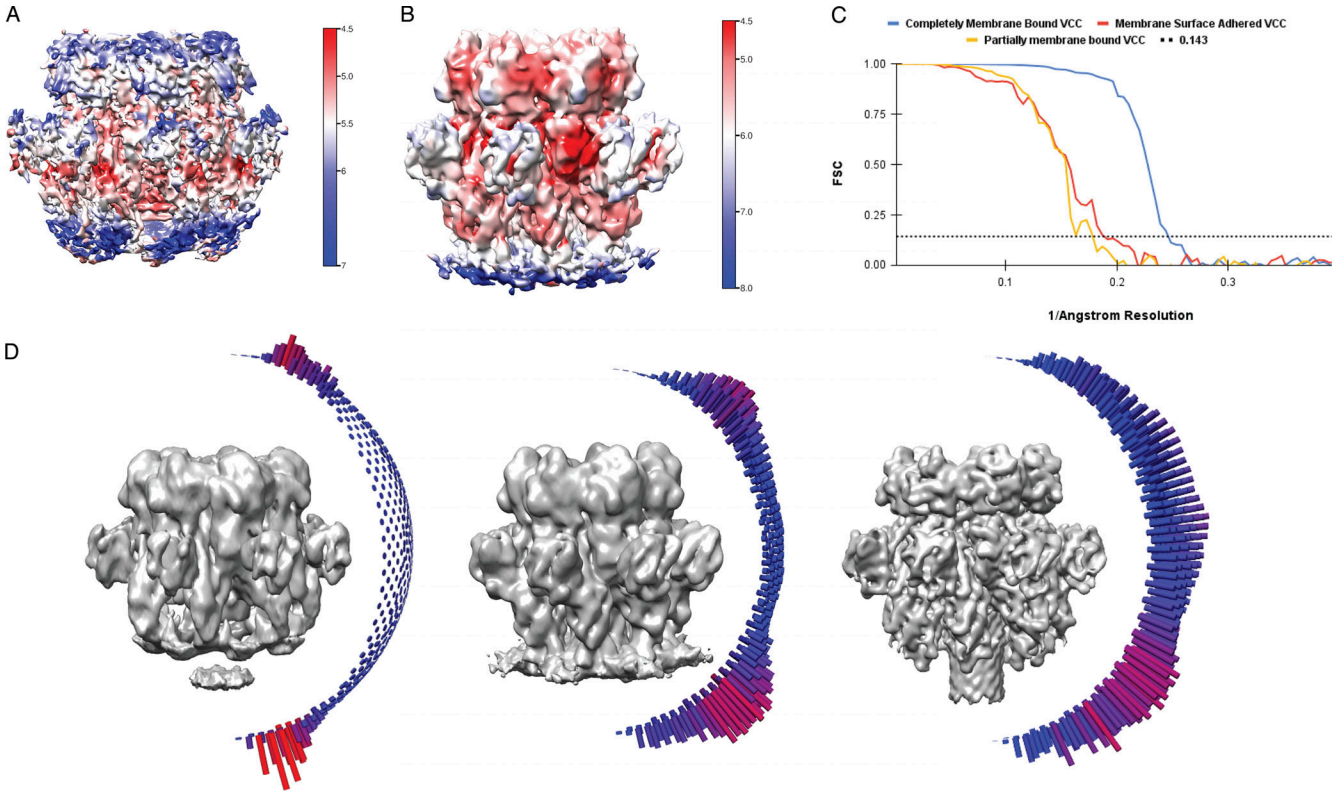

Figure S3. **Gold standard FSC calculation and assessment of overall map quality. (A)** Local resolution estimation of membrane surface–adhered VCC. **(B)** Local resolution estimation of partially membrane-bound VCC. **(C)** Graph showing FSC of the three maps estimated at 0.143. **(D)** Euler angle distribution of particles contributing to the three unique maps of VCC heptameric assembly.

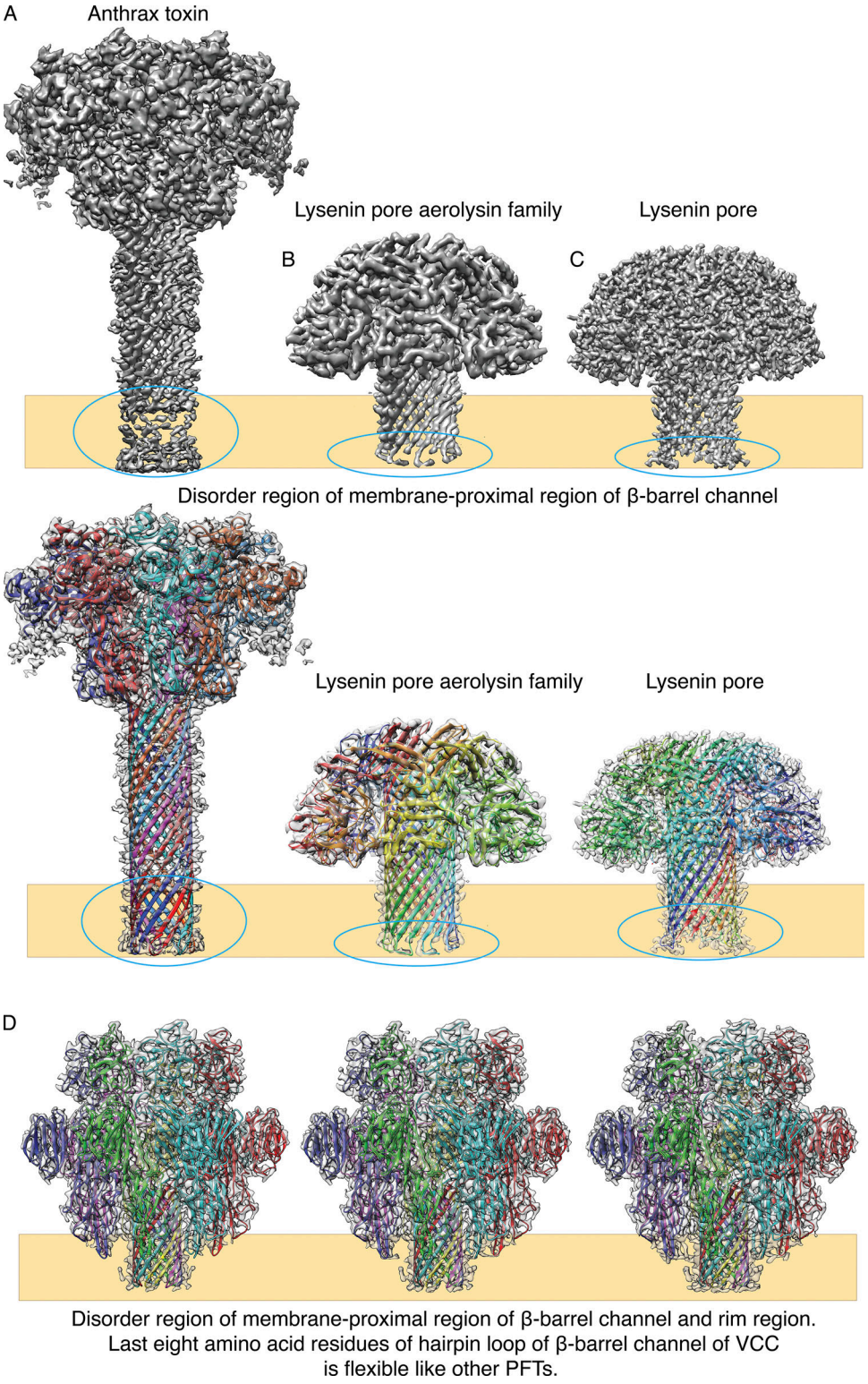

Figure S4. **Comparative analysis of the extent of disorder caused in the structure of PFTs by the presence of lipids. (A)** Cryo-EM map of anthrax toxin (Electron Microscopy Data Bank accession no. EMD-6224) placed on a cartoon lipid bilayer shows disorder in the transmembrane channel amino acid residues. **(B)** Cryo-EM map of lysenin toxin (Electron Microscopy Data Bank accession no. EMD-8015) placed on a cartoon lipid bilayer shows disorder in the transmembrane channel amino acid residues. **(C)** Density map of lysenin pore (PDB accession no. 5EC5) crystal structure shows disorder in the transmembrane channel amino acid residues. **(D)** Cryo-EM map of the completely lipid membrane–embedded VCC shows disorder in the last eight amino acids of the β-barrel.

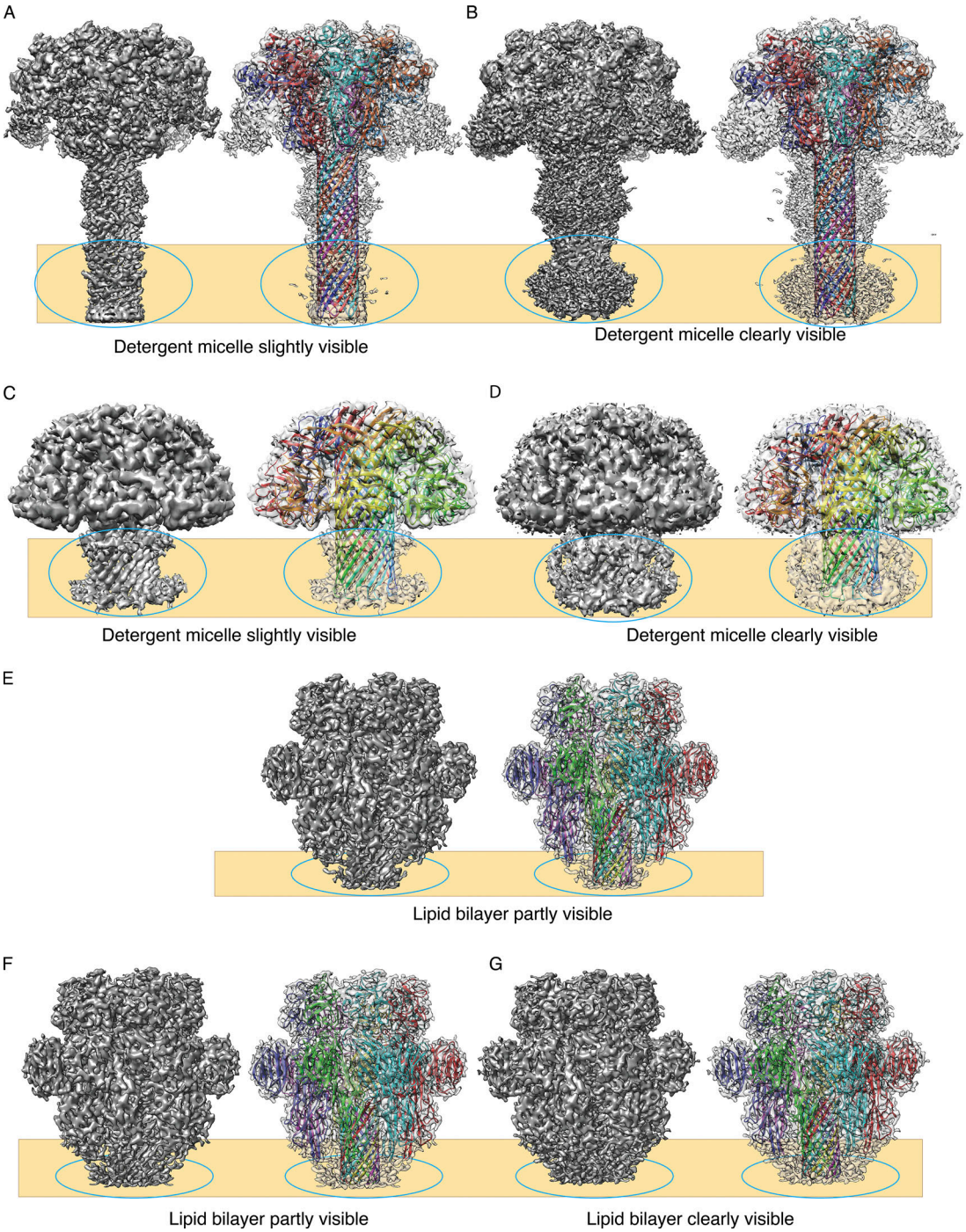

Figure S5. **Association of lipid moieties with membrane-interacting domains of PFTs. (A)** Appearance of faint density corresponding to detergent micelle on visualizing anthrax toxin (Electron Microscopy Data Bank accession no. EMD-6224, PDB under accession no. 3J9C) at a high threshold of volume. **(B)** Appearance of a prominent density corresponding to detergent micelle on visualizing anthrax toxin at a low threshold of volume. **(C)** Appearance of faint density corresponding to detergent micelle on visualizing lysenin toxin (Electron Microscopy Data Bank accession no. EMD-8015, PDB accession no. 5EC5) at a high threshold of volume. **(D)** Appearance of a prominent density corresponding to detergent micelle on visualizing lysenin toxin at a low threshold of volume. **(E)** Appearance of faint density corresponding to lipid bilayer on visualizing VCC at a low threshold of volume. **(F)** Increasingly prominent density of lipid bilayer observed on consecutively lowering the threshold of viewing VCC. **(G)** Further lowering the threshold of viewing shows the fully visible lipid bilayer where the rim domain of VCC is embedded in the membrane.

Video 1. **3D variability analysis of transmembrane channel of membrane bilayer–bound VCC.** Movie captured over frame 0 to frame 19 showing the continuous flexibility of the transmembrane barrel of VCC. Playback speed: 20 steps per second.

Video 2. **Top view representation for 3D variability analysis of membrane bilayer–bound VCC.** Movie captured over frame 0 to frame 19 showing overall flexibility in the distal mushroom-head–like architecture of VCC. Playback speed: 20 steps per second.